nature nanotechnology

SUPPLEMENTARY INFORMATION

DOI: 10.1038/NNANO.2015.336

Plasmonic nanofocused four-wave mixing for femtosecond near-field imaging

Vasily Kravtsov, Ronald Ulbricht, Joanna M. Atkin, and Markus B. Raschke*

E-mail: markus.raschke@colorado.edu

Dispersion compensation

To ensure transform-limited laser pulses shining on the tip grating, we compensate dispersion of the optical components using a multiphoton intrapulse interference phase scan (MIIPS) algorithm. A 20 μm thick BBO crystal is used in place of the tip (Supplementary Fig. 1), and the second harmonic generation (SHG) light is collected in transmission. The compensating spectral phase $\phi(\omega)$ is obtained iteratively with the MIIPS algorithm. Spectral amplitude and phase of the dispersion-compensated pulses are measured with an interferometric frequency-resolved optical gating (IFROG) using the same setup. We check that the retrieved spectral phase is flat, with residual second dispersion less than 10 fs^2.

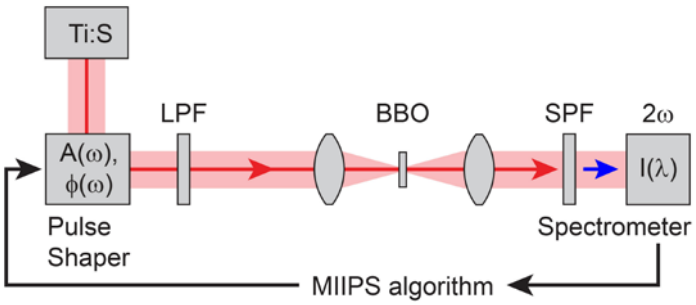

Supplementary Fig. 1: Schematic of the dispersion compensation procedure.

DOI: 10.1038/NNANO.2015.336

Non-resonant vs. resonant tip response

Four-wave mixing interferometric autocorrelation traces for a non-resonant (tip 1) and resonant (tip 2) cases are shown in Supplementary Fig. 2. Experimental data are shown as black symbols, and the simulation results are red lines. In (a), the experimental trace of tip 1 is best described by an instantaneous response. In contrast, for the tip 2 the response matches simulations with the dephasing time $T_2 = 11$ fs. The uncertainties are estimated to $\sim 2-3$ fs.

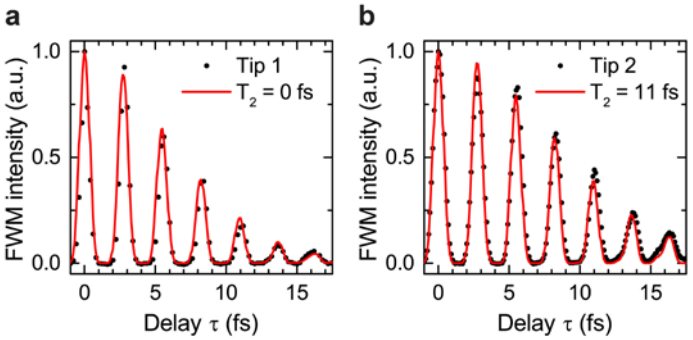

Supplementary Fig. 2: (a) Experimental FWM autocorrelation trace for tip 1 (symbols) and simulation with instantaneous response (line), experimental FWM autocorrelation trace for tip 2 (symbols) and simulation with dephasing time of 11 fs (line).

Nonlinear vs. linear imaging

Generation of nonlinear optical signal is key for nano-imaging with high sensitivity to the local electric field. Shown in Supplementary Fig. 3 are near-field optical images of the Au–Si step sample, taken simultaneously in two channels: (a) intra-pulse four-wave mixing (FWM) and (b) linear apex emission on the fundamental frequency. Shown in (c) are line cuts through the white dashed lines indicated in (a), (b). It is seen from both the images and line profiles that the nonlinear and linear signals demonstrate different behavior.

The linear signal in (b) is correlated with topography and does not show any "hot spots" as compared to the FWM image in (a). Further, the contrast for the fundamental signal is almost an order of magnitude lower than that of the FWM signal. These differences can be understood by

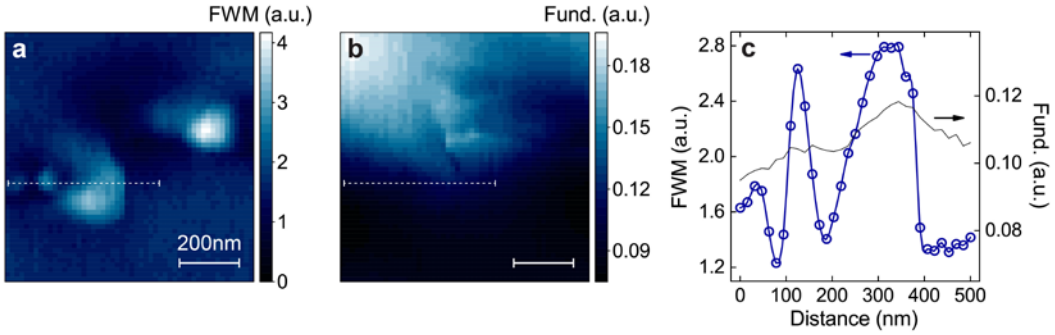

Supplementary Fig. 3: (a) FWM and (b) fundamental images. (c) Corresponding line profiles.

considering the generation mechanisms of the emitted signals. The fundamental response varies mostly due to the absorption in the sample and change in the radiation pattern, and therefore is only weakly dependent on the electric field in the tip–sample gap. In contrast, the FWM response is nonlinear in the local field, and therefore generated largely in the tip–sample gap, where the field is the strongest. This results in the higher contrast and sensitivity of the FWM signal as compared to the fundamental response.

Extraction of dephasing times

In order to extract dephasing time and resonant wavelength of the localized plasmonic modes observed in Fig. 4 in the main text, we simulate FWM autocorrelation traces I_{FWM} from the fundamental tip emission spectrum assuming resonant plasmon response, and find the best fit to the experimental data $I_i \pm \delta I_i$. We calculate the residual $r = \sum_i |I_{FWM} - I_i|/\delta I_i$ as a function of both dephasing time T_2 and resonant wavelength λ_0, as shown in Supplementary Fig. 4 for the two "hot spots" S1 (a) and S2 (b), with blue color indicating better fit. The two top branches in the 2D plots, corresponding to a particular resonant wavelength and arbitrary large T_2, are artifacts arising from the limited number of experimental data points. We exclude these regions from the analysis, based on the experimental evidence for the fast decay of the FWM signal with the inter-pulse delay. The resulting T_2 and λ_0 that provide the best fit are indicated in (a-b) by black dashed lines, with corresponding profiles for the residual shown in Supplementary Fig. 4c,d. From these pro-

DOI: 10.1038/NNANO.2015.336

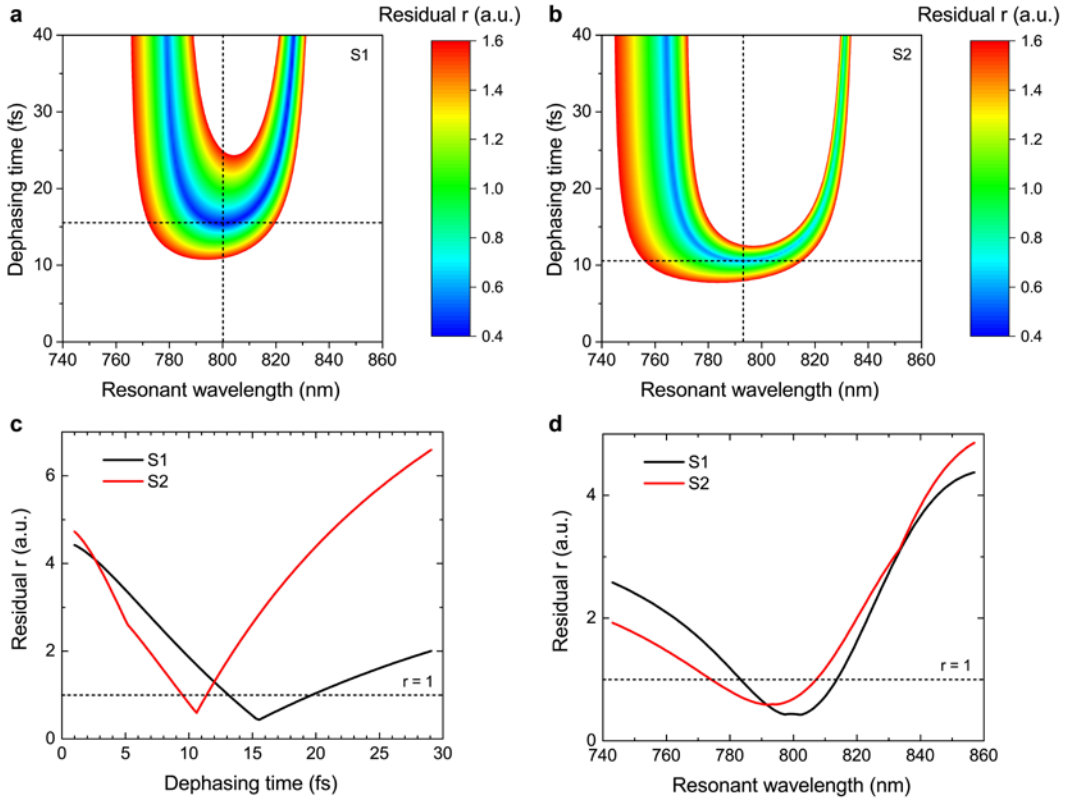

Supplementary Fig. 4: (a) Residual of the FWM autocorrelation fit as a function of dephasing time and resonant wavelength associated with plasmonic mode S1 and (b) S2, (c) profiles taken along vertical dashed lines in (a-b), (d) profiles taken along horizontal dashed lines in (a-b).

files we extract $T_2 = 16 \pm 3$ fs, $\lambda_0 = 800 \pm 20$ nm for the plasmonic mode S1, and $T_2 = 10 \pm 2$ fs, $\lambda_0 = 790 \pm 20$ nm for S2.

FWM field distribution

This section describes the calculation of the FWM efficiency as a function of tip apex radius. We use an ideal cone as a model of the tip, and calculate electric fields of the SPP using the adiabatic nanofocusing model.[1] Further, we assume that only the $m = 0$ azimuthal mode experiences nanofocusing and therefore gives rise to the FWM signal, and neglect contributions from other modes.

For a cylindrical plasmonic waveguide of radius R, using cylindrical coordinates, the amplitude of the transversal ($i = r$) or longitudinal ($i = z$) components of the SPP electric field can be expressed as:

$$E^{(i)}(\omega, r, z) = A^{(i)}(\omega, z)\mathscr{E}_{\mathrm{R}}^{(i)}(\omega, r), \tag{1}$$

with slowly varying envelope $A^{(i)}(\omega, z)$ and eigenmode $\mathscr{E}_{\mathrm{R}}^{(i)}(\omega, r)$.

We consider SPP field $\mathrm{E}_0^{(i)}(\omega_0, \vec{r})$ that induces a nonlinear polarization $\mathrm{P}_{\mathrm{FWM}}^{(i)}(\omega_{\mathrm{FWM}}, \vec{r})$. For the near-degenerate FWM process we can assume $\omega_{\mathrm{FWM}} \sim \omega_0$ in the following calculation.

The nonlinear polarization gives rise to the FWM electric field $\mathrm{E}_{\mathrm{FWM}}^{(i)}(\vec{r}, t)$ according to the nonlinear wave equation:

$$\nabla^2 \mathrm{E}_{\mathrm{FWM}}^{(i)}(\vec{r}, t) = \frac{1}{c^2}\frac{\partial^2 \mathrm{E}_{\mathrm{FWM}}^{(i)}(\vec{r}, t)}{\partial t^2} + \frac{1}{\varepsilon_0 c^2}\frac{\partial^2 \mathrm{P}_{\mathrm{FWM}}^{(i)}(\vec{r}, t)}{\partial t^2}. \tag{2}$$

Using coupled-mode theory in the slowly varying amplitude approximation,[2] we obtain a solution of Eq. 2 for the FWM electric field envelope:

$$\frac{\mathrm{dA}_{\mathrm{FWM}}^{(i)}(z)}{\mathrm{d}z} = -\frac{ik_0}{2n_{\mathrm{eff}}\varepsilon_0} \cdot \frac{\int_0^\infty \mathrm{P}_{\mathrm{FWM}}^{(i)}(\vec{r})\mathscr{E}_{\mathrm{R}}^{(i)}(r) r\,\mathrm{d}r}{\int_0^\infty \left[\mathscr{E}_{\mathrm{R}}^{(i)}(r)\right]^2 r\,\mathrm{d}r}, \tag{3}$$

with effective refractive index n_{eff} and free-space wave vector $k_0 = \omega_0/c$.

For the nonlinear polarization, we consider an isotropic response in the form $\mathrm{P}_{\mathrm{FWM}}^{(i)}(\vec{r}) = \varepsilon_0 \chi^{(3)} \left[\mathrm{E}_0^{(i)}(\vec{r})\right]^3$. For the case of FWM generation on a cone, we assume a slowly varying radius $R = R(z)$, and write the FWM field generated by the original SPP field $\mathrm{E}_0^{(i)}(\vec{r})$ at the surface

DOI: 10.1038/NNANO.2015.336

($r = R$) at an arbitrary point along the z-axis:

$$dE_{FWM}^{(i)}(R,z) = -\frac{ik_0\chi^{(3)}E_0^{(i)}(R,z)}{2n_{eff}(z)} \cdot \frac{\int_0^R \left[E_0^{(i)}(r,z)\right]^4 r\,dr}{\int_0^\infty \left[E_0^{(i)}(r,z)\right]^2 r\,dr} dz. \quad (4)$$

Electric field $E_0^{(i)}(r,z)$ and effective refractive index $n_{eff}(z)$ are calculated using the adiabatic model of nanofocusing. To take into account the nanofocusing of the generated FWM, we note that, according to the adiabatic model, an SPP launched at the point z with the electric field $E^{(i)}(z)$ will contribute to the electric field at point z_1:

$$E^{(i)}(z_1) = \frac{f(z_1)}{f(z)} e^{-\mathrm{Im}\int_z^{z_1} n_{eff}(z')k_0\,dz'} E^{(i)}(z), \quad (5)$$

with the exponential factor due to damping, and $f(z)$ due to compression of the SPPs. The resulting FWM field at the point z_1 is calculated by integrating over all contributions that are generated during the SPP propagation along the cone:

$$E_{FWM}^{(i)}(R(z_1),z_1) = \int_{z_0}^{z_1} \frac{f(z_1)}{f(z)} e^{-\mathrm{Im}\int_z^{z_1} n_{eff}(z')k_0\,dz'} dE_{FWM}^{(i)}(R(z),z). \quad (6)$$

From the FWM electric field, we calculate the FWM efficiency according to:

$$\eta(R) = \left|\frac{E_{FWM}(R,z(R))}{E_0(R,z(R))}\right|^2. \quad (7)$$

The FWM field and efficiency depend on the initial electric field of the SPP launched on the cone surface. With ~ 10 kW of peak power incident on the grating, and $\sim 1\%$ coupling efficiency, we estimate the initial E-field of the SPP in the experiment to be ~ 200 MV/m. We use an estimate for the Au nonlinear susceptibility $\chi^{(3)} \sim 10^{-19}$ m^2/V^2 from literature,[3] with only the intraband contribution due to low photon energy (1.5 eV), and neglecting the hot-electron contribution due

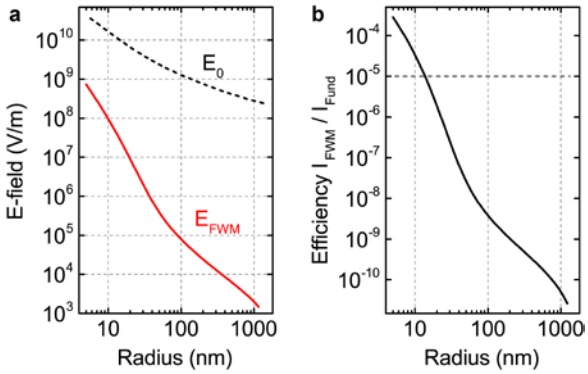

Supplementary Fig. 5: (a) Electric fields of the SPP and FWM as functions of termination point radius *R*, calculated using adiabatic nanofocusing model for tip angle 8° and launching SPP 15 μm from the apex. (b) FWM efficiency as a function of radius R. Gray dashed line indicates the maximum efficiency observed in the experiment.

to ultrashort ∼ 10 fs pulses. The fields calculated for a cone with half apical angle of 10°, and SPPs launched 15 μm away from the apex, are shown in Supplementary Fig. 5a. The corresponding FWM efficiency is shown in Supplementary Fig. 5b, with the gray dashed line indicating the maximum efficiency observed in the experiment.

The FWM on the tip is a phase-matched process. While the signal is generated predominantly at the near-apex region, and therefore is determined by the local field enhancement at the apex, the overall distribution of the surface plasmon field on the tip contributes to the signal strength. This can result in a slightly different tip angle for maximizing FWM compared to that for maximizing the apex field enhancement.

References

(1) Stockman, M.I. Nanofocusing of optical energy in tapered plasmonic waveguides. *Phys. Rev. Lett.* **93**, 137404 (2004).

(2) Yariv, A. Coupled-mode theory for guided-wave optics. *IEEE J. Quantum Electron.* **9**, 919–933 (1973).

DOI: 10.1038/NNANO.2015.336

(3) Boyd, R.W., Shi, Z. & De Leon, I. The third-order nonlinear optical susceptibility of gold. *Opt. Commun.* **326**, 74–79 (2014).